Surface Engineering for Enhanced Perovskite Solar Cells: Fullerene-Mediated Trap State Formation on $CsPbI_3$ (001) Surface

Gibu George[a], Dmitry I. Sharapa[b], Anton J. Stasyuk[a], Albert Poater[a], Miquel Solà[a]*, and Sergio Posada-Pérez[a]*

[a]Institut de Química Computacional i Catàlisi and Departament de Química, Universitat de Girona, c/ Maria Aurèlia Capmany 69, 17003 Girona, Catalonia, Spain.
[b]Institute of Catalysis Research and Technology (IKFT), Karlsruhe Institute of Technology, Eggenstein-Leopoldshafen, 76344, Germany.

Corresponding authors: Miquel Solà (miquel.sola@udg.edu) Sergio Posada-Pérez (sergio.posada@udg.edu)

Abstract

Photovoltaic technology, particularly perovskite solar cell (PSC) materials, has emerged as a promising avenue due to their excellent light-absorbing properties. Despite significant progress in PSC technology, defects within the perovskite material continue to pose challenges, leading to reduced efficiency and stability of the devices. $CsPbI_3$ perovskites have shown potential, but trap states induced by surface defects remain a challenge. The use of fullerene-derivatives, like C_{60} and $PC_{61}BM$, has been highlighted to enhance the device stability eliminating/reducing hysteresis and passivating trap states. However, the mechanisms behind fullerene-induced passivation of trap states and their impact on surface energetics remain unclear. This study employs periodic density functional theory (DFT) simulations to explore the interaction between C_{60}, $PC_{61}BM$, and $CsPbI_3$ (001) surface, with and without defects (cesium vacancy, lead vacancy, and I-antisite). The DFT simulations reveal that both C_{60} and $PC_{61}BM$ effectively passivate trap states induced by I-antisite defects by reorienting and reorganizing the iodine atoms that promote the presence of trap states. This work contributes to understanding the fundamental aspects of surface-defect interactions in $CsPbI_3$ perovskites. Both C_{60} and $PC_{61}BM$ play a crucial role in passivating trap states, causing atomic reorganization and avoiding the nonradiative recombination. The findings provide valuable insights into mechanisms for trap state passivation by fullerene derivatives, paving the way for further research to enhance PSC performance.

Keywords: Perovskites ● Solar cells ● Fullerenes ● Trap states ● Surface passivation ● Cs perovskites

Introduction

Boosting renewable energies is the 7th goal of 17 sustainable development goals (SDGs) of the 2030 United Nations Agenda for Sustainable development. The 7th SDG is a plan of action for people, planet and prosperity whose premise is to accelerate the transition towards a low-carbon competitive economy. Currently, electricity generated from fossil fuels (coal, gas, and oil) exceeds 60%, while renewable energy sources contribute about 7-9 % of global energy use.[1] To achieve carbon neutrality, it is imperative to reverse the tendency of the global energy production towards the use of renewable energy sources. Recognizing solar power as the largest exploitable energy resource has driven the extraordinary growth of photovoltaic (PV) cell technology to meet increasing energy demands. Perovskite solar cell (PSC) materials have garnered significant attention in the field of PV due to their exceptional light-absorbing properties and ease of fabrication.[2–10] The inception of PSCs dates back to the early 2000s, when researchers began exploring organic-inorganic hybrid PSCs as potential candidates for converting sunlight into electricity.[11] Currently, the maximum efficiency reported for PSCs is 26.7 %.[3,12–14]

One of the main issues with organic-inorganic PSCs is their decomposition due to volatile organic cations.[15,16] One of the strategies to solve this problem is the use of inorganic cations to improve the PSC stability.[17,18] $CsPbI_3$ perovskites emerged as promising materials for solar cell applications,[19–21] demonstrating charge-carrier mobilities comparable to those of organic-inorganic PSCs, presenting efficiencies over 20%.[22] Additionally, with a Goldshmidt tolerance factor favorable for cubic perovskites,[23–26] $CsPbI_3$ is a stable perovskite structure with slight distortions that prone to some degree of structural deformation. Although PSCs have achieved a maximum reported efficiency of 26.7%, this is still below the theoretical limit of approximately 33% for single-junction devices under standard test conditions.[27] This discrepancy can be attributed to the formation of defects during the perovskite crystallization process. The presence of defects is commonly related to the nonradiative recombination of the electron-hole pair, mainly due to the formation of trap states, prompting a decay in the PSCs performance.[28–36]

$CsPbI_3$ perovskites exhibit various defects including vacancies, uncoordinated cations, and antisite defects on their surfaces and interfaces.[37–42] Vacancies occur when an ion is missing from its lattice site, interstitial defects occur when an ion occupies an interstitial position, and antisite defects are generated when an atom or ion takes the place of another

atom or ion at a different site within the crystal lattice. Defects located on the perovskite surfaces may induce alterations in the coordination environment of the atoms.[35] These defects, including anion-cation antisites, may form deep traps for charge carriers at different energy levels and can significantly affect device performance. The intrinsic point defects can introduce covalent bonds (as new bonds can form between the defect-generating atoms and the atoms in the perovskite unit cell), forming structures like I-I-I trimers. These species generate deep trap states within the bandgap, serving as recombination centers for photogenerated carriers.[43–45] These surface defects are more frequent than bulk defects,[33,46] although recent studies show that halide vacancies primarily generate bulk traps.[47]

Since the pioneering work of Jeng and coworkers in 2013,[48] the use of fullerene-derivatives as electron transport layer or additives has generated a lot of attention. They have eliminated/reduced the hysteresis,[49–52] improved the device stability in comparison to fullerene-free standard PSCs,[53–55] and favors the high-scale preparation. Furthermore, it is well-known the capability of fullerene-derivatives to passivate trap states, and defects [56] as well as other molecules like benzene or pyridine.[57] For instance, Huang et al. revealed that the inclusion of $PC_{61}BM$ on the methylammonium lead perovskite films mitigated trap states, enhancing the power conversion efficiency from 7.3% to around 14.9%.[49] In addition, $PC_{61}BM$ was proposed as an additive able to passivate rich-iodide defects and several other trap states at the grain boundaries of $CH_3NH_3PbI_3$,[50] favoring the charge collection.[58,59] Li and collaborators proved that $PC_{61}BM$ was able to suppress trap states formed by Pb-I antisites,[50] and an identical conclusion was achieved by Loi and coworkers. They propose that fullerenes can assist the recombination of trap states on methylammonium lead perovskite.[60] A similar passivation effect has been reported by several authors using C_{60}. Fu et al. showed that C_{60} end-capped with polyethylene glycol was able to passivate defects of perovskite films,[61] same behavior observed after the functionalization of C_{60} with pyridine,[62] thiophene, cyano,[63] and indene-C_{60} groups.[64] Li and coworkers incorporated a triblock fullerene derivative between TiO_2 and perovskite, enhancing charge extraction, and passivating interface defects.[65]

Despite the experimentally demonstrated positive effect of fullerene derivatives on the PSC devices, it is not clear and not well understood how fullerenes passivate these trap states, the effect of binding groups of fullerenes, and how passivation influences the

surface energetics. Further studies are needed to better understand the fullerene-perovskite interactions to develop more efficient and stable devices. Notably, very few computational studies have explored these interactions, and none have comprehensively addressed the effects of the most common defects in the perovskite lattice and the mechanism related with the defect's passivation.[66] By means of periodic density functional theory (DFT) simulations, we have investigated the interaction of C_{60} and $PC_{61}BM$ with $CsPbI_3$ (001) surface with and without defects (cesium vacancy, lead vacancy, and I-antisite). These systems were selected due to their significant relevance in both fundamental research and practical applications. C_{60} and $PC_{61}BM$, as well-established fullerene derivatives, are particularly relevant because they have demonstrated promising passivation effects in perovskite solar cells, and their interaction with perovskites is still not fully understood. These systems present an ideal starting point for future studies aimed at optimizing perovskite-based devices through defect engineering and fullerene-based passivation. Our simulations unveil how both C_{60} and $PC_{61}BM$ can eliminate the trap state generated by the I-antisite since they promote the surface reconstruction of the perovskite.

Computational details and models

Periodic DFT calculations were performed with the Vienna Ab initio Simulation Package (VASP) code.[67] Optimizations were performed using the Perdew-Burke-Ernzerhof (PBE) exchange-correlation functional,[68] including the D3 formalism of Grimme, since van der Waals interactions play a major role in the description of fullerene reactivity[69] and fullerene-perovskite interaction.[66,70] It is important to mention that PBE is highly accurate to calculate the binding energies and to describe the surface geometry,[71] surface-adsorbate interactions, making it a reliable choice for studying these perovskite systems. Additionally, the versatility of the PBE functional when enhanced with van der Waals corrections ensures a balanced treatment of bonding interactions and dispersion forces, which are crucial for modeling hybrid organic-inorganic perovskites.[72] Nevertheless PBE usually underestimates the bandgap of the materials.[73] However, the bandgap is accurately predicted for several perovskite[74] and oxide materials due to a fortuitous cancellation of errors between relativistic, spin-orbit coupling, and electronic correlation.[75,76] The presence of heavy atoms necessitates the proper treatment of relativistic effects with spin orbit coupling (SOC)[77,78] albeit with a tradeoff between computational accuracy and cost. The Green's function method (GW) is computationally

intensive,[33,79] and hybrids are a good alternative, although considering the size of our systems, this level of theory is not feasible. Therefore, we use PBE-D3 to describe the perovskite interaction and compute the binding energy, charge density differences, and projected density of states (PDOS). The most relevant systems have been reoptimized considering SOC, although no remarkable differences were found in the PDOS, i.e., the presence (or not) of trap states is independent of the method used.[80] The electronic density of the valence electrons was expanded onto a plane-wave basis set. The effects caused by the core electrons on the valence ones were described through the projected augmented wave (PAW) method of Blöch[81] as implemented by Kresse and Joubert.[82] For the electronic relaxation, the system is considered converged when the total energy change was smaller than 10^{-5} eV. For the atomic relaxation, the minimization is reached when the forces acting on the atoms were smaller than 0.01 eV $Å^{-1}$.

To perform the simulations, we have selected the cubic structure which has a band gap of 1.73 eV, suitable for solar cells.[83] The lowest energy and maximum exposed surface, (001), which is the major facet of halide perovskites, has been chosen.[19] Our slab model is a 3×3 supercell of a CsI terminated surface with 6 layers (3 CsI and 3 PbI_2 layers) having 135 atoms (see SI for further details). The two outermost layers have been relaxed, allowing the atomic displacement. All the defects induced on the neutral slab are reported in Table 1. According to Kye and coworkers,[84] the formation of cation vacancies plays a critical role in stabilizing the cubic phase of $CsPbI_3$. This stabilization is supported by the formation of cation vacancies, favored by the use of I-rich conditions.[84] For this reason, we have modelled slabs that contain cationic vacancies and the occupation of one iodine atom in the Pb site. The formation of the cesium and lead vacancies have been performed by extracting one cesium atom from the most external layer and one lead from the second one. The surface with I-antisite contains one extra iodine substituting one lead atom on the second layer. The presence of these mentioned defects comes with a charge neutrality loss of the PSC slab. One approach to ensure charge neutrality of the slab is by intentionally introducing spatially localized countercharges into the system.[85] In our case, we have included alkali Li atoms on the bottom layer of the defective slabs to compensate the charged surface, thereby avoiding the need for charged cells. The Li atoms were placed on the bottom of the slab and we allow their optimization, maintaining the CsI and PbI_2 layers frozen. Once the geometry was optimized, the alkali ions were

kept frozen during the optimization of the surface energy and the adsorption of the fullerene derivatives thereon.

Table 1: Defects investigate in this work, summarizing the atoms removed (A_{out}), the atoms incorporated (A_{in}), the charge of the perovskite surface, and the number of Li placed on the bottom layer to compensate the charge.

Defect	A_{out}	A_{in}	Charge	Li	Modelling
Cs_{vac}	Cs	-	-1	1	One of the external Cs atoms was removed
Pb_{vac}	Pb	-	-2	2	One of the Pb atoms located in the second layer was removed
I-antisite	Pb	I	-3	3	One of the Pb atoms located in the second layer was exchanged by one I atom

The binding energy of the C_{60} and $PC_{61}BM$ has been computed according to eq. 1:

$$E_{ads} = E_{F/surf} - (E_{surf} + E_f) \quad (1)$$

where $E_{F/surf}$ is the total DFT energy of the fullerene adsorbed on the surface, E_f is the energy of the isolated fullerene, and E_{surf} is the energy of the corresponding surface, with or without defects. For the currently studied systems, the charge distribution is estimated by the QTAIM method of Bader.[86]

Results

Generation of surface defects on $CsPbI_3$ (001)

First, the stoichiometric slab geometry was optimized to ensure a structurally accurate representation of the defect-free surface. Subsequently, the common defects described in Table 1 were systematically modeled by introducing them into the optimized slab, followed by additional structural relaxations to capture the resulting surface reconstructions. Figure 1a depicts the optimized structure of $CsPbI_3$ (001) and its corresponding PDOS. During the optimization process, the most external cesium atoms shifted downward by 0.8 Å (Figure S3a, SI).

The subsequent step has been to induce the surface defects. The formation of cesium vacancy on the most exposed surface layer does not lead to distortion of the slab geometry. From the point of view of the electronic structure, the PDOS plot did not reveal significant differences with respect to the $CsPbI_3$ (001) surface without defects (Figure S3b, SI). On the other hand, removing one of the lead atoms from the second layer does not produce significant variations in the surface geometry and electronic structure, as encountered

with cesium vacancy (Figure S3c, SI). Nevertheless, the presence of an I-antisite defect leads to alterations in both electronic structure and surface geometry. First of all, we found two configurations, quasi-degenerate in energy (only 0.15 eV between them). During the optimization process, the iodine that replaces lead on the second layer shifts upwards (referred to as **I1 site**), moving closer to the outermost CsI layer (Figure 1b). Subsequently, one of the iodine atoms, originally aligned with cesium atoms on the first layer, migrates upwards to bind with two cesium atoms (referred to as **I42 site**) on the outermost layer. The PDOS analysis clearly shows the formation of a trap state in the middle of the bandgap associated with **I42** atom situated on top of cesium atoms. This is not unexpected since it has been reported that this kind of defects promote the formation of these states[87] and is as well reported how fullerenes can passivate them.[50] The presence of the I-antisite defect does not directly trigger the formation of the trap state but induces structural changes on the surface, leading to the generation of these trap states between the valence and the conduction band (CB) of the perovskite. We referred to this slab as **$CsPbI_3$-I-antisite-TRAP**. On the other hand, we found a second slab structure that is 0.15 eV lower in energy. In this case, our DFT simulations unveiled a novel surface reconstruction (referred to as **$CsPbI_3$-I-antisite-NoTRAP**) where the iodine atom located on top of two cesium on **$CsPbI_3$-I-antisite-TRAP** model (**I42**), moves downwards to the surface and connects with one of the lead atoms located on the second layer, which moves upwards. Apart from the slightly favored energetics, this model does not show the presence of trap states (see Figure 1c). Due to the short energy difference and the importance of the presence of trap states, both slabs have been considered to evaluate the C_{60} and $PC_{61}BM$ adsorption thereon.

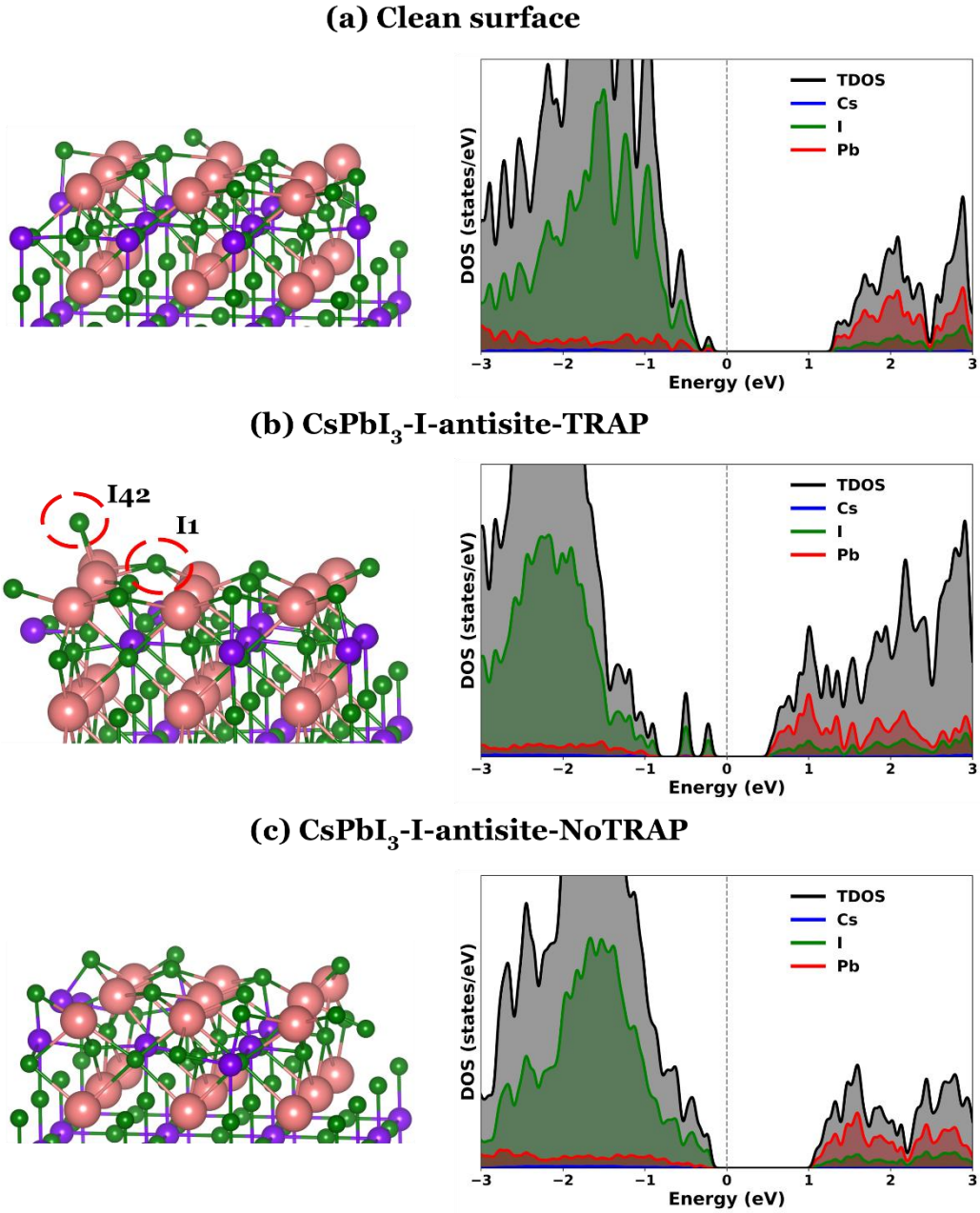

Figure 1. (a) Optimized geometry of $CsPbI_3$ surface without defects (left) and the corresponding projected density of states (right), (b) reconstructed structure (**$CsPbI_3$-I-antisite-TRAP**) of $CsPbI_3$ (001) with I-antisite (**I1**) (left) and the corresponding PDOS of the same surface with focus on the **I42** site causing trap state (right). (c) reconstructed structure (**$CsPbI_3$-I-antisite-NoTRAP**) of $CsPbI_3$ (001) with I-antisite (left) and the corresponding PDOS of the same surface (right).

C_{60}-$CsPbI_3$ and $PC_{61}BM$-$CsPbI_3$ Interaction

The initial step in this study involved exploring the interaction of the two fullerenes under investigation with the stoichiometric $CsPbI_3$ (001) surface, meaning no defects were included in this phase of the analysis. Figure 2 illustrates the four different orientations of C_{60} considered for its interaction with the CsI-terminated $CsPbI_3$ (001) slab, with

positions on top of cesium (TopCs) and on top of iodine (TopI). This includes hexagonal (*hex*) and pentagonal (*pen*) faces, as well as two specific types of carbon-carbon (C–C) bonds that connect two hexagons or one hexagon and one pentagon face, namely *bond66* and *bond65*, respectively. Throughout the optimization process, no drastic changes in geometry were observed for any of the configurations. Table 2 reports the binding energies of C_{60}, displaying the influence of the adsorption surface site. These values are around 0.3-0.4 eV lower (i.e., weaker interaction) with respect the values encountered for C_{60} adsorption on methylammonium lead perovskite.[66] The adsorption on top of the cesium atoms is energetically preferred compared to the adsorption on TopI. The C_{60} is closer to the surface when it is placed on TopCs (Figure S4, SI). The sinking of the most external cesium atoms of the first surface layer allows the enclosure of C_{60} between the four iodine atoms neighboring to the cesium site. In contrast, the adsorption on TopI implies large distances (around 0.9-1 Å with respect TopCs geometries) to the CsI layer. The charge density difference analysis, as illustrated in Figure S5 (see SI), revealed an accumulation of electron density between cesium and C_{60}, suggesting more attractive interaction with respect to iodine surface atoms, where a depletion of electron density is observed. Notably, the orientation of C_{60} does not show remarkable differences in the binding energy values. Specifically, when adsorbed on TopCs site, the four different orientations exhibit a maximum energy difference of 0.03 eV, while it was 0.04 eV on TopI site. These findings suggest that C_{60} can be accommodated on the surface in diverse orientations.

On the other hand, the Bader charge exploration shows minimal charge transfer from the surface to the C_{60} (only 0.04 e^-). Our analysis of the PDOS did not reveal any significant difference since the bands of the perovskite appear at the same energies with respect to the Fermi level independent of the presence of the C_{60}. Moreover, no remarkable differences were found comparing the distinct C_{60} orientations and adsorption sites (see Figure S6, SI, for the systematic comparison).

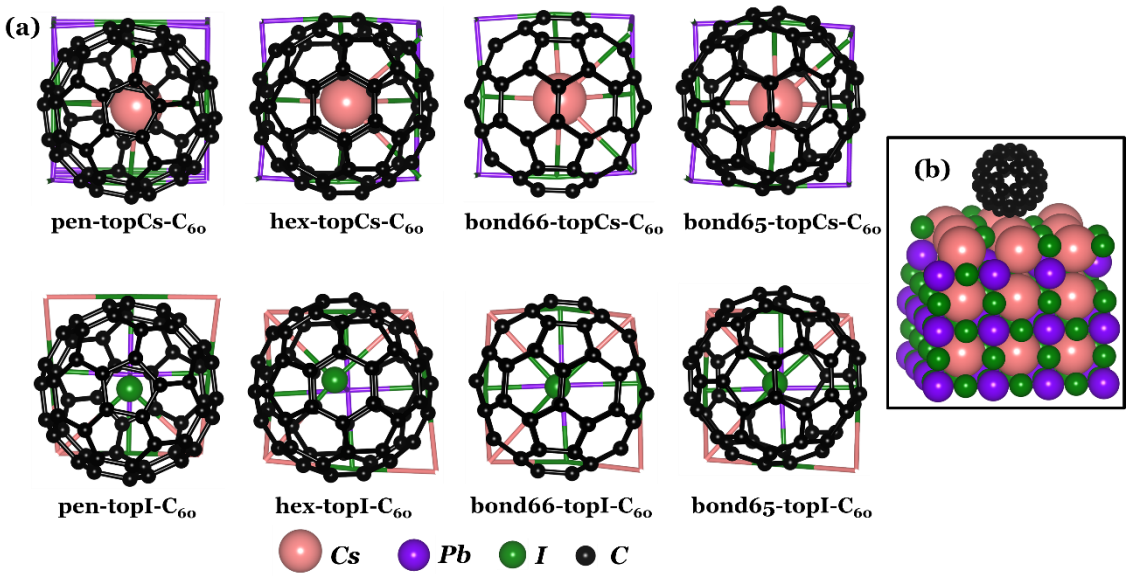

Figure 2. (a) Studied different orientations of C_{60} with CsI-terminated $CsPbI_3$ (001) slab, on top of cesium (TopCs) and on top of iodine (TopI). (b) a representation of C_{60} adsorbed on the clean $CsPbI_3$ slab.

Table 2. Binding energies (in eV) for different orientations of C_{60} on top of cesium and iodine on CsI-terminated $CsPbI_3$ slab.

Binding energies		
Orientation of C_{60}	**TopCs**	**TopI**
hex-C_{60}	-0.59	-0.41
pen-C_{60}	-0.56	-0.41
bond66-C_{60}	-0.56	-0.37
bond65-C_{60}	-0.58	-0.39

The identical procedure employed for C_{60} has been used to investigate the interaction between $CsPbI_3$ (001) surface and $PC_{61}BM$. The primary distinction between C_{60} and $PC_{61}BM$ lies in the functional group. For $PC_{61}BM$, a few more orientations should be considered to evaluate the effect of this functional group. This includes the interaction of $PC_{61}BM$ in two main orientations: being perpendicular and parallel to the surface *via* different orientations of fullerene cage as well as the functional group moieties (Figure 3).

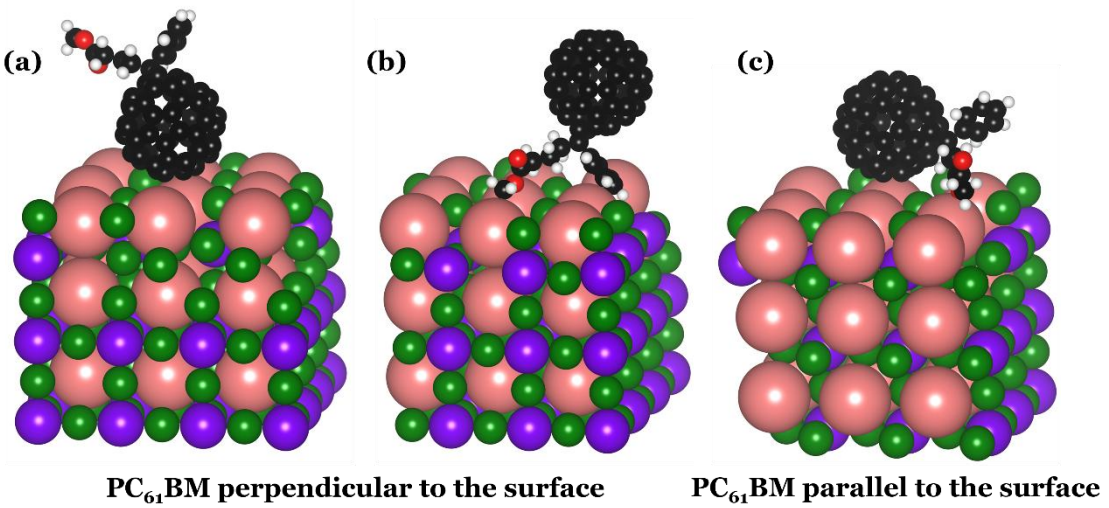

Figure 3. Representation of distinct orientations of $PC_{61}BM$ in which; (a) $PC_{61}BM$ is perpendicular to the slab where the fullerene cage is in direct contact with the slab, (b) $PC_{61}BM$ is perpendicular to the slab where the functional group moiety is in direct contact with the slab, and (c) $PC_{61}BM$ is parallel to the slab.

The binding energies of the considered orientations are listed in Table 3. Note that only configurations adsorbed on TopCs have been considered, based on the results obtained for C_{60}. When the $PC_{61}BM$ is oriented perpendicular to the surface and the contact with $CsPbI_3$ (001) is by means of the fullerene cage, a similar behavior to that observed for C_{60} is seen. However, the binding energy values for $PC_{61}BM$ are slightly more negative (~-0.75 eV). It is noteworthy that the orientation of the fullerene cage (*pen/hex* face or *bond 66/65*) does not play a significant role, since the binding energy values are almost the same. The PDOS analysis did not show remarkable differences with respect to the bare $CsPbI_3$ (001) surface without fullerenes (Figure S7, SI).

Table 3. Binding energies (in eV) for different orientations of $PC_{61}BM$ on top of clean $CsPbI_3$ slab.

Binding energies	
$PC_{61}BM$ perpendicular to the surface [a]	
hex-perp-$PC_{61}BM$	-0.75
pen-perp-$PC_{61}BM$	-0.70
bond66-perp-$PC_{61}BM$	-0.71
bond65-perp-$PC_{61}BM$	-0.72
$PC_{61}BM$ perpendicular to the surface [b]	
oxy-perp-$PC_{61}BM$	-0.50

phenyl-oxy-perp-$PC_{61}BM$	-0.92
$PC_{61}BM$ parallel to the surface	
hex-para-$PC_{61}BM$	-1.22
pen-para-$PC_{61}BM$	-1.21

[a] fullerene cage in direct contact with the surface.
[b] functional group moieties in direct contact with the surface.

Furthermore, we have explored the direct contact between the functional group and the surface, being the C_{60} cage far from the perovskite. As reported in Table 3, when the carbonyl oxygen atom of the ester functional group is bonded to one of the cesium atoms, the binding energy is weaker (-0.50 eV) compared to the scenario where the phenyl group is adsorbed on the perovskite surface, being the binding energy almost twice higher (-0.92 eV). For both cases, PDOS plots (Figure S7, SI) illustrate that the second CB of the $PC_{61}BM$ is higher in energy with respect to the CB of the perovskite, in contrast to the other $PC_{61}BM$ orientations. This fact can be attributed to the larger distance between the carbon cage and the perovskite since this band corresponds to the atoms on the fullerene cage rather than the functional group (Figure S8, SI). This suggests that the interaction of the fullerene cage with the perovskite surface slightly displace the second CB to lower energy values. Finally, the strongest interaction was found orienting the $PC_{61}BM$ parallel to the surface, maximizing the number of $PC_{61}BM$-surface contacts. A binding energy of -1.22 eV was found. Nevertheless, it has not significantly affected the PDOS analysis since it shows the same PDOS plot as the other configurations with weaker binding energies.

C_{60} and $PC_{61}BM$ Interaction with $CsPbI_3$ defective surface

To provide a comprehensive analysis, we have investigated the impact of surface defects (Cs_{vac}, Pb_{vac}, and I-antisite) on the interaction of $CsPbI_3$ perovskite surface and the fullerenes studied in this work. The binding energies of C_{60} are reported in Table 4. Note that the energy reference of the surface is the total energy of the slab after the formation of the defect. For the surface featuring a single cesium vacancy (Cs_{vac}), we have evaluated and compared the adsorption of C_{60} at three specific sites: directly on top of the Cs_{vac}, on TopI, and on top of one of the Cs atoms neighboring the Cs_{vac}. Our conformational analysis reveals that C_{60} preferentially adsorbs on top of the Cs_{vac}. The adsorption at the nearby TopI sites exhibits a further reduction in binding energy (around 0.40 eV). This difference is much higher than the difference found on the defect-free perovskite (see

Table 2), indicating that the vacancy significantly impacts the interaction with C_{60}. On the other hand, when the C_{60} is placed over one of the cesium atoms neighboring the vacancy, the binding energy decreases by approximately 0.30 eV compared to the adsorption on top of Cs_{vac}. This trend was consistently observed across all tested C_{60} orientations, and for this reason, they are not included in Table 4. Thus, all the systems in Table 4 labelled as TopCs corresponds to the adsorption of C_{60} on top of the Cs_{vac}. The strongest binding energy observed, -0.83 eV, is more than 0.2 eV higher than the interaction with the defect-free perovskite.

Furthermore, the PDOS analysis of both orientations (over Cs_{vac} and over neighboring Cs) shows slight differences that are important to highlight. When the C_{60} is adsorbed on top of the vacancy, the second CB of the C_{60} overlaps with the conduction band minima (CBM) of the perovskite (Figure 4a). According to the results from Cui and coworkers,[88] this fact strongly suggests fast interfacial electron transfer from the perovskite to C_{60}. However, the adsorption on the adjacent TopCs slightly displaces the second CB of C_{60} to lower energy, being not aligned with the CBM of the perovskite (Figure 4b). This difference could affect the electron transfer process, essential for the performance of the solar cell device. Thus, the presence of the Cs vacancy enhances the binding energy resulting in a more favorable electronic structure that promotes the electron transfer process, as highlighted in the work of Cui and collaborators.

On the other hand, the presence of lead vacancy does not show remarkable variations in the surface geometry and the electronic structure of the system. The binding energy values are quite similar to those for C_{60} adsorption on the $CsPbI_3$ (001) surface without vacancies and are slightly lower than those for a slab with a cesium vacancy. In this scenario, the adsorption of C_{60} on TopI site is not significantly different in terms of energetics from adsorption on TopCs. Details about the PDOS plots for cesium and lead vacancies can be found in Figure S9, SI.

Table 4. Lowest binding energies (in eV) for each different orientations of C_{60} on top of cesium and on top of iodine on CsI-terminated $CsPbI_3$ slab with three defects.

Binding energies				
Systems	**Cs vacancy** [a]	**Pb vacancy**	**I-antisite**	
	E_{ads}	E_{ads}	E_{ads}	E_{rel} [b]

hex-topCs-C_{60}	-0.79	-0.54	-0.69	0.09
hex-topCs-C_{60}-TRAP	-	-	-0.62	0.30
pen-topCs-C_{60}	-0.83	-0.51	-0.64	0.13
bond66-topCs-C_{60}	-0.74	-0.51	-0.64	0.13
bond65-topCs-C_{60}	-0.83	-0.51	-0.68	0.10
hex-topI-C_{60}	-0.37	-0.32	-0.58	0.19
pen-topI-C_{60}	-0.35	-0.38	-0.77	0.00
bond66-topI-C_{60}	-0.34	-0.50	-0.29	0.48
bond65-topI-C_{60}	-0.35	-0.53	-0.22	0.55

[a] Systems labelled as TopCs correspond to C_{60} adsorbed over the Cs vacancy.
[b] E_{rel} is the relative energy of the system where the lowest energy (absolute) system (**pen-topI-C_{60}**) is taken as the reference.

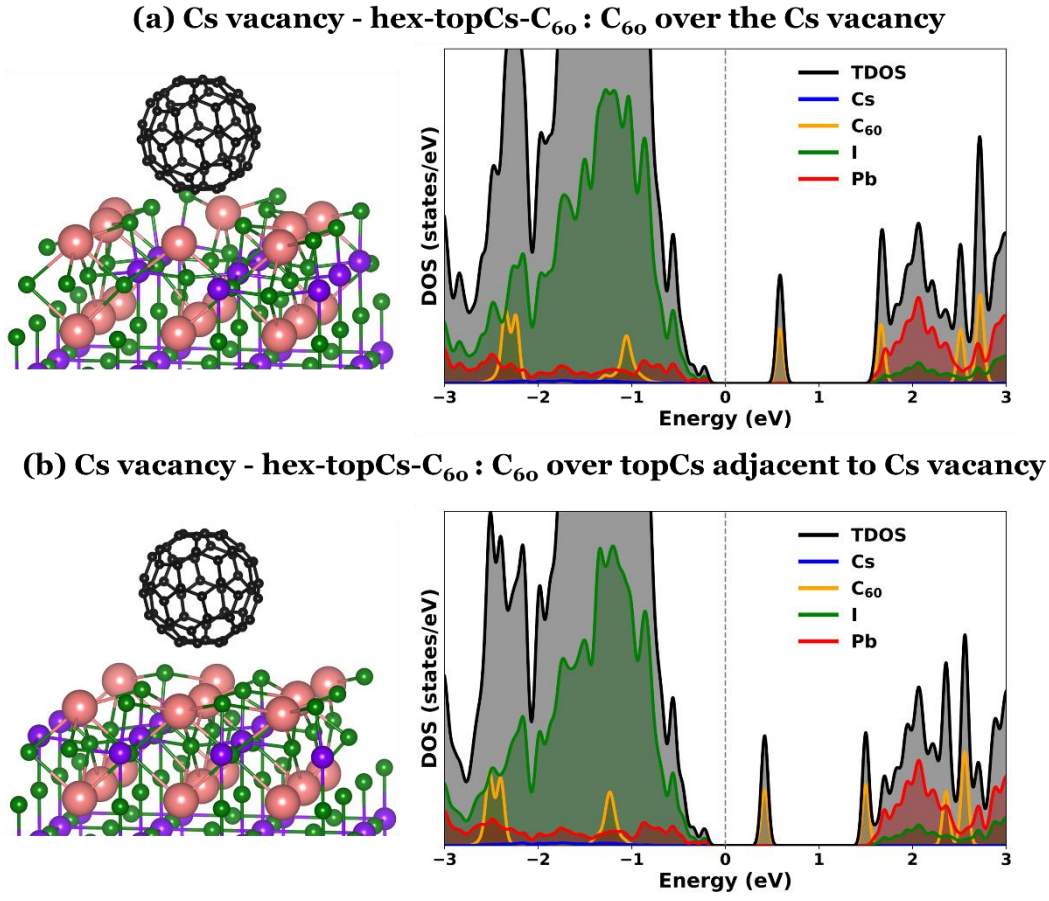

Figure 4. Optimized geometry of C_{60} adsorbed on $CsPbI_3$ surface with cesium vacancy, where (**a**) C_{60} is on top of the vacant site; (**b**) C_{60} is on top of the cesium atom adjacent to the vacancy site and their corresponding total and PDOS plots.

Regarding the formation of I-antisites, we have considered the two different surface configurations illustrated in Figure 1, **$CsPbI_3$-I-antisite-TRAP,** and **$CsPbI_3$-I-antisite-NoTRAP.** The first one comes with a surface reconstruction where one of the iodine atoms shift upwards into the CsI layer inducing the presence of a trap state in the middle of the bandgap. In contrast, the latter do not show this iodine atom displacement and the associated trap states are only 0.15 eV lower in energy. The C_{60} has been initially placed on TopCs and TopI atoms on both (almost) energetically equivalent slabs. All the C_{60} adsorption geometries investigated on **$CsPbI_3$-I-antisite-NoTRAP** system preserved the initial surface geometry, i.e., without the presence of trap states. Interestingly, when the C_{60} adsorbs onto the **$CsPbI_3$-I-antisite-TRAP** configuration, our DFT simulations revealed, in the majority of the tested cases, a surface reconstruction towards **$CsPbI_3$-I-antisite-NoTRAP** configuration. As detailed in Tables S1 and S2, no significant structural differences were observed in the outermost surface layers when compared to the adsorption of C_{60} on defect-free surfaces. Aside from the displaced iodine atom, the rest of the cation-anion distances on the surface remain largely unaffected. The only notable change is observed for the Cs-I bond distances within the topmost layer, where systems with trap states exhibit slightly shorter distances (~0.3-0.4 Å). This occurs because, in the **$CsPbI_3$-I-antisite-TRAP** configuration, the iodine atom occupies a position on top of the most exposed layer, creating a vacancy in this region. This is compensated by the shortening of bond distances between iodine and cesium atoms.

The presence of C_{60} promotes the displacement of the iodine atom to the outermost layer**,** reconstructing the surface configuration and removing the associated trap states as well. In Table 4, the binding and relative energies of the adsorption on **$CsPbI_3$-I-antisite-NoTRAP** are reported. These systems exhibit the most favorable relative energies and adsorption energies in comparison to the configurations with trap states. In other words, the system without trap states is energetically more stable, regardless of the orientation and adsorption site of C_{60}. The strongest binding energy of -0.77 eV is achieved, with several C_{60} orientations exhibiting very similar relative energies, indicating they can be considered energetically degenerate. The PDOS plot revealed that the trap state is no longer present (Figure 5a), since the iodine atom that promotes their formation is anchored to the outermost layer connected with one of the lead atoms located on the second layer. At this particular case, the transference of charge from the surface to the C_{60} is quantified at 0.14 e^-.

It is important to note that we found one configuration (**hex-topCs-C_{60}-TRAP)** that retains the reconstructed **$CsPbI_3$-I-antisite-TRAP** surface with its trap state, despite C_{60} adsorption. This system shows a relative energy of 0.30 eV (see Table 4) compared to the most stable system without trap states. Prior to the C_{60} adsorption, the difference in energy between **$CsPbI_3$-I-antisite-TRAP** to **$CsPbI_3$-I-antisite-NoTRAP** slabs was 0.15 eV, being the latter the lowest in energy, while the presence of C_{60} increases this difference 0.15 eV more. In Figure 5b, this configuration is illustrated, where the **I42** atom remains in place, maintaining the trap states. Indeed, the PDOS analysis clearly revealed the presence of the trap states associated to this iodine atom. In this specific case, the iodine atom is not re-anchored to the CsI layer, thus inducing the presence of trap states. However, according to our simulations, these trap states do not significantly impact charge transfer, which is quantified as $0.11e^-$ form the surface to the C_{60}.

With the goal to explore the direct interaction between the reconstructed iodine atom on top of the CsI layer, we modelled a new adsorption geometry where the C_{60} was placed on top of the **I42** atom. Interestingly, the initial structural geometry of **$CsPbI_3$-I-antisite-TRAP** was preserved after the energy minimization process. However, this configuration is not energetically competitive, being more than 0.60 eV higher in energy with respect to the lowest energy system (Figure S10, SI). This is because the C_{60} does not induce, in this particular case, the surface reconstruction and the elimination of the trap state. The C_{60} is placed on top of the iodine atom, far from the surface and minimizing the surface-adsorbate contacts. All of this makes this configuration irrelevant.

In summary, the presence of C_{60} can effectively passivate the I-antisite induced defect, increasing the energy difference between configurations without and with trap states since the adsorption of C_{60} induces the surface reconstruction with the subsequent elimination of the trap states.

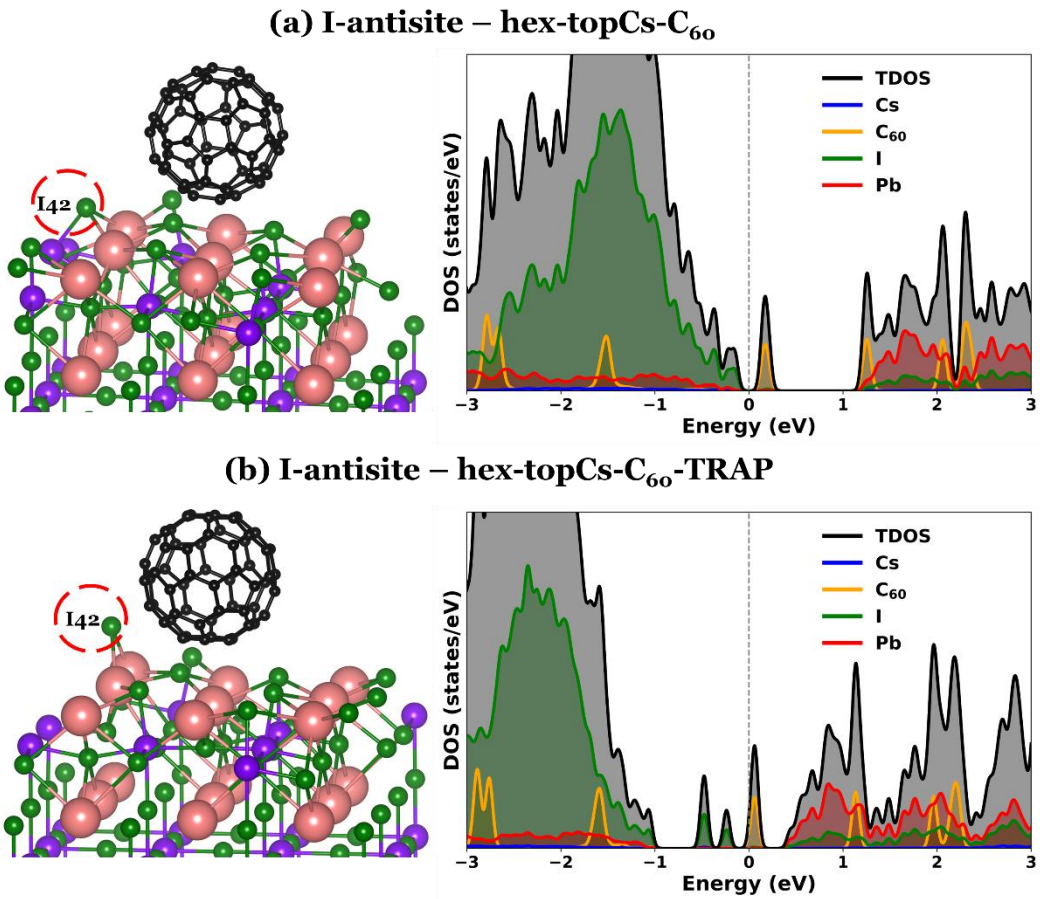

Figure 5. (a) C_{60}-$CsPbI_3$ system with I-antisite defect and the corresponding total and PDOS plot that passivate the trap state. (b) C_{60}-$CsPbI_3$ system with I-antisite defect and the corresponding total and PDOS plot, showing the trap state associated with the iodine atom (**I42 site**).

The investigation was also extended to the interaction with $PC_{61}BM$ with the three different defects considered in this study. Table 5 reports the binding energies, with $PC_{61}BM$ exhibiting an attractive interaction with the defective surfaces. The preferred surface orientation continues to be the parallel alignment of $PC_{61}BM$, maximizing contact points with the surface. As observed for C_{60} adsorption, the presence of cesium vacancy comes with a slightly stronger interaction between the surface and the $PC_{61}BM$ (around 0.15 eV more negative with respect to defect-free perovskite). This increment in the binding energy is observed for parallel and perpendicular (fullerene cage) orientations, while the adsorption energy is almost equivalent when the functional group is in direct contact with the surface.

In the context of the I-antisite defect, the perpendicular adsorption of $PC_{61}BM$ exhibits the weakest binding energies. Concerning the lowest energy systems, adsorbed in parallel to the surface, we have observed both surface geometries, **$CsPbI_3$-I-antisite-TRAP** and **$CsPbI_3$-I-antisite-NoTRAP.** The lowest energy configuration, with a calculated binding energy of -1.30 eV, shows the functional group of $PC_{61}BM$ pointing to the **I42** site (Figure 6a) promoting its displacement downwards and passivating the trap state, as depicted in the PDOS plot, where no trap state in the middle of the bandgap is observed. On the other hand, with a 0.18 eV of difference (Table 5), our simulations reveal that in **hex-para-$PC_{61}BM$-TRAP** configuration, when the fullerene cage is adsorbed adjacent to the **I42** position, the iodine atom remains unchanged (Figure 6b). Notably, the reconstruction towards **$CsPbI_3$-I-antisite-NoTRAP** configuration is not observed. The PDOS analysis confirms the presence of the trap states associated with the **I42** site. Interestingly, our DFT simulations reveal the importance of the orientation of $PC_{61}BM$ with respect to the defects; the functional group is able to promote the displacement of the iodine that induces the trap states, while the direct contact of this iodine with the carbon cage does not modify the position of the iodine, allowing the presence of trap states in the middle of the bandgap. Therefore, the surface engineering and the deposition of the adsorbate play a crucial role in the passivation of trap states.

Table 5. Binding energies (in eV) for different orientations of $PC_{61}BM$ on top of cesium on CsI-terminated $CsPbI_3$ surface with three defects.

Binding energies				
$PC_{61}BM$ perpendicular to the surface [a]				
	Cs vacancy	***Pb vacancy***	**I-antisite**	
Systems	E_{ads}	E_{ads}	E_{ads}	E_{rel} [b]
hex-perp-$PC_{61}BM$	-0.81	-0.60	-0.58	0.72
pen-perp-$PC_{61}BM$	-0.80	-0.66	-0.75	0.55
bond66-perp-$PC_{61}BM$	-0.78	-0.67	-0.11	0.92
bond65-perp-$PC_{61}BM$	-0.82	-0.65	-0.56	0.74
$PC_{61}BM$ perpendicular to the surface [c]				
oxy-perp-$PC_{61}BM$	-0.44	-0.49	-0.33	0.97

phenyl-oxy-perp-PC$_{61}$BM	-0.92	-0.98	-0.67	0.63
PC$_{61}$BM parallel to the surface				
hex-para-PC$_{61}$BM [d]	-1.36	-1.23	-1.30	0.00
hex-para-PC$_{61}$BM-TRAP [e]	-	-	-1.27	0.18
pen-para-PC$_{61}$BM	-1.37	-1.23	-1.14	0.16

[a] fullerene cage in direct contact with the surface.
[b] E_{rel} is the relative energy of the system where the lowest energy (absolute) system (**hex-para-PC$_{61}$BM** with the functional group pointing to the **I42** site) is taken as the reference.
[c] functional group moieties in direct contact with the surface.
[d] the functional group is pointing to the **I42** site.
[e] the carbon cage is pointing to the **I42** site. This configuration has been only computed for I-antisite systems due to the presence of **I42** out of the CsI plane. The binding energy has been computed using the energy of **CsPbI$_3$-I-antisite-TRAP** as reference. For the rest of the systems, the energy of **CsPbI$_3$-I-antisite-NoTRAP** slab has been considered.

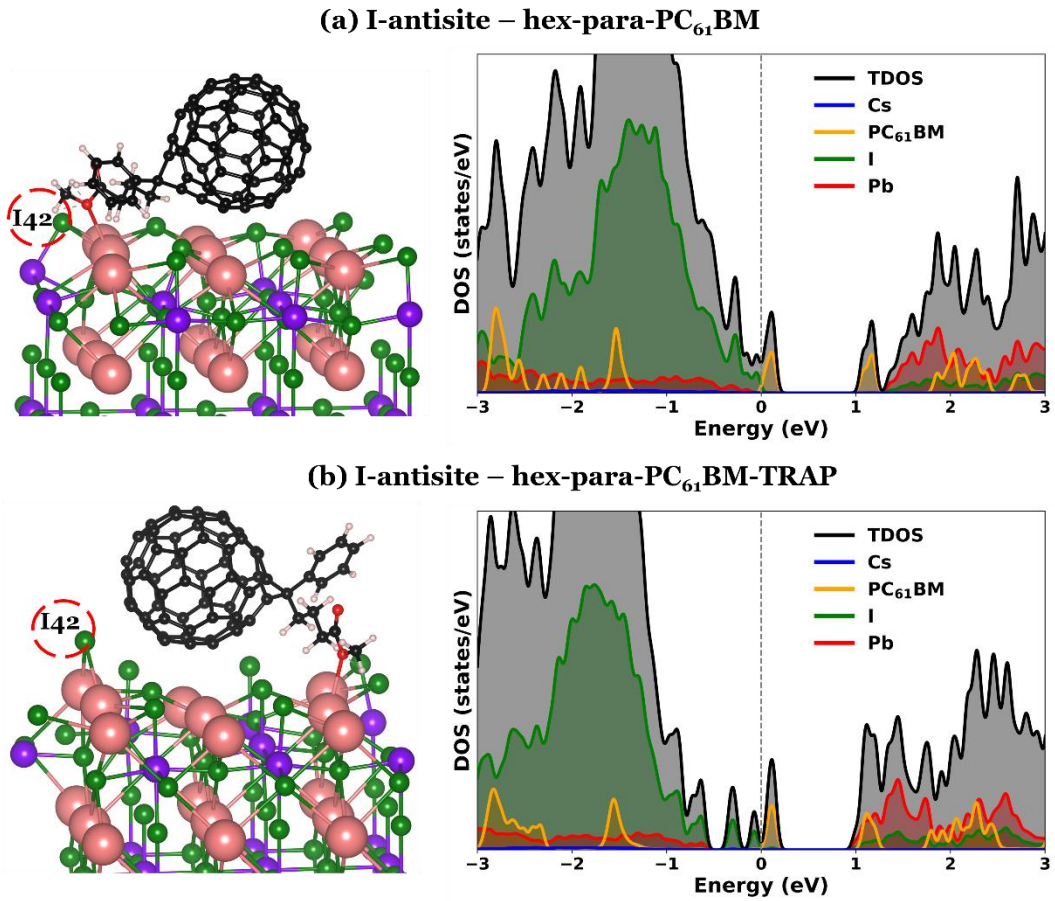

Figure 6. (a) Sketch and PDOS of $PC_{61}BM$-$CsPbI_3$ (001) with I-antisite system without trap state. (b) Sketch and PDOS of $PC_{61}BM$-$CsPbI_3$ with I-antisite maintaining the trap state.

The effect of adsorbing fullerene derivatives on $CsPbI_3$ (001) surface can be summarized as follows. Adsorption of both C_{60} and $PC_{61}BM$ on defect-free surfaces results in attractive interactions without significantly altering the electronic structure. The presence of cesium and lead vacancies leads to slight variations in binding energies; specifically, direct contact between the carbon cages of the fullerene and a cesium vacancy slightly enhances (i.e., makes more attractive) the binding energies, while binding energies remain largely unchanged when adsorption occurs on slabs with lead vacancy sites. The introduction of an I-antisite defect results in two nearly degenerate structures following energy minimization. One geometry, which is 0.15 eV higher in energy, that generates trap states within the bandgap due to the upward migration of an iodine atom to the outermost layer. When the C_{60} is adsorbed on this surface with trap states, the majority of geometries favor a surface reconstruction that eliminates the trap states. The only optimized structure that retains iodine at the surface after C_{60} adsorption is 0.30 eV higher in energy, thereby increasing the energy difference between the surface with and without trap states. A similar effect is observed upon adsorption of $PC_{61}BM$, which adsorbs parallel to the surface with both the carbon cage and the functional group in contact with the surface. When the functional group is oriented towards the iodine atom that induces trap states, the iodine moves downward into the CsI layer, eliminating the trap state. This configuration is the lowest in energy. The trap state is only retained when the carbon cage is directed towards the iodine atom.

Conclusions

Periodic DFT simulations have been employed to study the interaction between C_{60}, $PC_{61}BM$, and $CsPbI_3$ perovskite (001) surface, shedding light on their potential role in passivating trap states induced by surface defects. Our findings indicate that both C_{60} and $PC_{61}BM$ can help to diminish trap states arising from I-antisite defects, promoting surface reconstruction, and can enhance electron transfer processes.

Through comprehensive DFT calculations, we elucidated the structural and electronic changes induced by surface defects such as cesium and lead vacancies, and I-antisite defects on the $CsPbI_3$ (001) surface. The presence of I-antisite on bare surface comes with a surface reorganization that generates a trap state in the middle of the bandgap, being this surface only 0.15 eV higher than the surface without surface reconstruction, and thus, without trap states

The adsorption of both C_{60} and $PC_{61}BM$ was examined on the CsI termination of $CsPbI_3$ (001) surface with and without defects. The binding energies on non-defective surface show attractive interaction with both fullerenes, with $PC_{61}BM$ exhibiting the largest binding energies (-1.21 eV) when placed parallel to the surface, maximizing the surface-adsorbate contacts. The adsorption of both C_{60} and $PC_{61}BM$ on surface containing defects, implies more attractive interactions when they are placed on top of the cesium vacancy. Our simulations suggest that both fullerenes hinder the formation of trap states associated with I-antisite defects. Both C_{60} and $PC_{61}BM$ induce the reconstruction of the iodine atom increasing the energy difference between the surface without and with traps (0.30 and 0.18 eV respectively).

This study provides a theoretical framework for understanding how fullerene derivatives, such as C_{60} and $PC_{61}BM$, can passivate surface defects in $CsPbI_3$ perovskites, a critical factor in improving solar cell performance. The research highlights how surface defects, particularly I-antisites, create trap states that negatively affects charge transport in perovskite solar cells. By focusing on how fullerenes interact with these defects, the study aids experimentalists in selecting materials for surface treatment, optimizing fabrication conditions, and improving device efficiency.

Acknowledgments

G.G. is thankful for the contract 2020 FISDU 00345 from the Generalitat de Catalunya and the mobility grant (MOB2021) from the Universitat de Girona. S.P.-P. appreciates the economic support of Marie Curie fellowship (H2020-MSCA-IF-2020-101020330). A.P. is a Serra Húnter Fellow and received the ICREA Academia Prize 2019. M.S. and A.P. thank the Spanish MCIN (MCIN/AEI/10.13039/50110001103) for projects PID2023-147424NB-I00, PID2020-13711GB-I00, PGC2018-097722-B-I00, and RED2022-134331-T, and the Generalitat de Catalunya for project 2021SGR623. Computational time at the MARENOSTRUM supercomputer has been provided by the Barcelona Supercomputing Centre through a grant from Red Española de Supercomputación, projects QHS-2021-3-0009, QHS-2022-1-0016, and QHS-2022-3-0001 and also by the Consorci de Serveis Universitaris de Catalunya (CSUC). We also acknowledge the support by Baden-Württemberg through bwHPC (bwUniCluster and bwForCluster JUSTUS).

References

[1] BPstats, BP Statistical Review of World Energy. https://www.bp.com/content/dam/bp/business-sites/en/global/corporate/pdfs/energy-economics/statistical-review/bp-stats-review-2018-full-report.pdf, 2018 (accessed 01 October 2024).

[2] H.S. Jung, N.-G. Park, Perovskite Solar Cells: From Materials to Devices, Small 11 (2015) 10–25. https://doi.org/https://doi.org/10.1002/smll.201402767.

[3] J.Y. Kim, J.-W. Lee, H.S. Jung, H. Shin, N.-G. Park, High-Efficiency Perovskite Solar Cells, Chem. Rev. 120 (2020) 7867–7918. https://doi.org/10.1021/acs.chemrev.0c00107.

[4] N.-G. Park, Perovskite solar cells: an emerging photovoltaic technology, Mater. Today 18 (2015) 65–72. https://doi.org/https://doi.org/10.1016/j.mattod.2014.07.007.

[5] W.S. Yang, B.-W. Park, E.H. Jung, N.J. Jeon, Y.C. Kim, D.U. Lee, S.S. Shin, J. Seo, E.K. Kim, J.H. Noh, S. Il Seok, Iodide management in formamidinium-lead-halide–based perovskite layers for efficient solar cells, Science 356 (2017) 1376–1379. https://doi.org/10.1126/science.aan2301.

[6] M. Liu, M.B. Johnston, H.J. Snaith, Efficient planar heterojunction perovskite solar cells by vapour deposition, Nature 501 (2013) 395–398. https://doi.org/10.1038/nature12509.

[7] D.B. Mitzi, Introduction: Perovskites, Chem. Rev. 119 (2019) 3033–3035. https://doi.org/10.1021/acs.chemrev.8b00800.

[8] A.K. Jena, A. Kulkarni, T. Miyasaka, Halide Perovskite Photovoltaics: Background, Status, and Future Prospects, Chem. Rev. 119 (2019) 3036–3103. https://doi.org/10.1021/acs.chemrev.8b00539.

[9] J. Tian, Q. Xue, Q. Yao, N. Li, C.J. Brabec, H.-L. Yip, Inorganic Halide Perovskite Solar Cells: Progress and Challenges, Adv. Energy Mater. 10 (2020) 2000183. https://doi.org/https://doi.org/10.1002/aenm.202000183.

[10] M. Saliba, J.-P. Correa-Baena, M. Grätzel, A. Hagfeldt, A. Abate, Perovskite Solar Cells: From the Atomic Level to Film Quality and Device Performance,

Angew. Chem. Int. Ed. 57 (2018) 2554–2569. https://doi.org/https://doi.org/10.1002/anie.201703226.

[11] A. Kojima, K. Teshima, Y. Shirai, T. Miyasaka, Organometal Halide Perovskites as Visible-Light Sensitizers for Photovoltaic Cells, J. Am. Chem. Soc. 131 (2009) 6050–6051. https://doi.org/10.1021/ja809598r.

[12] H. Min, D.Y. Lee, J. Kim, G. Kim, K.S. Lee, J. Kim, M.J. Paik, Y.K. Kim, K.S. Kim, M.G. Kim, T.J. Shin, S. Il Seok, Perovskite solar cells with atomically coherent interlayers on SnO_2 electrodes, Nature 598 (2021) 444–450. https://doi.org/10.1038/s41586-021-03964-8.

[13] NREL, Best research-cell efficiency chart. https://www.nrel.gov/pv/cell-efficiency.html, 2022 (accessed 01 October 2024).

[14] Y. Tian, X. Zhang, K. Zhao, X. Miao, T. Deng, W. Fan, D. Jin, X. Jiang, S. Zhong, X. Wang, S. Wang, P. Shi, L. Tian, L. Yao, S. Gong, X. Yu, X. Gao, Z. Chen, X. Chen, Y. Lu, V. Shrote, Y. Yang, D. Yang, R. Wang, J. Xue, High-entropy hybrid perovskites with disordered organic moieties for perovskite solar cells, Nat. Photonics 18 (2024) 960–966. https://doi.org/10.1038/s41566-024-01468-1.

[15] J.A. Christians, P.A. Miranda Herrera, P. V Kamat, Transformation of the Excited State and Photovoltaic Efficiency of $CH_3NH_3PbI_3$ Perovskite upon Controlled Exposure to Humidified Air, J. Am. Chem. Soc. 137 (2015) 1530–1538. https://doi.org/10.1021/ja511132a.

[16] E.J. Juarez-Perez, Z. Hawash, S.R. Raga, L.K. Ono, Y. Qi, Thermal degradation of $CH_3NH_3PbI_3$ perovskite into NH_3 and CH_3I gases observed by coupled thermogravimetry–mass spectrometry analysis, Energy Environ. Sci. 9 (2016) 3406–3410. https://doi.org/10.1039/C6EE02016J.

[17] N.A.N. Ouedraogo, Y. Chen, Y.Y. Xiao, Q. Meng, C.B. Han, H. Yan, Y. Zhang, Stability of all-inorganic perovskite solar cells, Nano Energy 67 (2020) 104249. https://doi.org/https://doi.org/10.1016/j.nanoen.2019.104249.

[18] H. Zhu, S. Teale, M.N. Lintangpradipto, S. Mahesh, B. Chen, M.D. McGehee, E.H. Sargent, O.M. Bakr, Long-term operating stability in perovskite photovoltaics, Nat. Rev. Mater. 8 (2023) 569–586.

https://doi.org/10.1038/s41578-023-00582-w.

[19] Z. Yao, W. Zhao, S. (Frank) Liu, Stability of the $CsPbI_3$ perovskite: from fundamentals to improvements, J. Mater. Chem. A 9 (2021) 11124–11144. https://doi.org/10.1039/D1TA01252E.

[20] X. Tan, S. Wang, Q. Zhang, H. Liu, W. Li, L. Zhu, H. Chen, Stabilizing $CsPbI_3$ perovskite for photovoltaic applications, Matter 6 (2023) 691–727. https://doi.org/https://doi.org/10.1016/j.matt.2022.12.012.

[21] S. Lim, S. Han, D. Kim, J. Min, J. Choi, T. Park, Key Factors Affecting the Stability of $CsPbI_3$ Perovskite Quantum Dot Solar Cells: A Comprehensive Review, Adv. Mater. 35 (2023) 2203430. https://doi.org/https://doi.org/10.1002/adma.202203430.

[22] S.M. Yoon, H. Min, J.B. Kim, G. Kim, K.S. Lee, S. Il Seok, Surface Engineering of Ambient-Air-Processed Cesium Lead Triiodide Layers for Efficient Solar Cells, Joule 5 (2021) 183–196. https://doi.org/https://doi.org/10.1016/j.joule.2020.11.020.

[23] Z. Li, M. Yang, J.-S. Park, S.-H. Wei, J.J. Berry, K. Zhu, Stabilizing Perovskite Structures by Tuning Tolerance Factor: Formation of Formamidinium and Cesium Lead Iodide Solid-State Alloys, Chem. Mater. 28 (2016) 284–292. https://doi.org/10.1021/acs.chemmater.5b04107.

[24] D. Ji, S. Feng, L. Wang, S. Wang, M. Na, H. Zhang, C. Zhang, X. Li, Regulatory tolerance and octahedral factors by using vacancy in $APbI_3$ perovskites, Vacuum 164 (2019) 186–193. https://doi.org/https://doi.org/10.1016/j.vacuum.2019.03.018.

[25] D. Liu, W. Zha, Y. Guo, R. Sa, Insight into the Improved Phase Stability of $CsPbI_3$ from First-Principles Calculations, ACS Omega 5 (2020) 893–896. https://doi.org/10.1021/acsomega.9b03838.

[26] K. Sekar, R. Manisekaran, O.M. Nwakanma, M. Babudurai, Significance of Formamidinium Incorporation in Perovskite Composition and Its Impact on Solar Cell Efficiency: A Mini-Review, Adv. Energy Sustain. Res. 5 (2024) 2400003. https://doi.org/https://doi.org/10.1002/aesr.202400003.

[27] W. Shockley, H.J. Queisser, Detailed Balance Limit of Efficiency of p-n Junction Solar Cells, J. Appl. Phys. 32 (1961) 510–519. https://doi.org/10.1063/1.1736034.

[28] Y. Yuan, J. Huang, Ion Migration in Organometal Trihalide Perovskite and Its Impact on Photovoltaic Efficiency and Stability, Acc. Chem. Res. 49 (2016) 286–293. https://doi.org/10.1021/acs.accounts.5b00420.

[29] R. Long, O. V Prezhdo, Dopants Control Electron–Hole Recombination at Perovskite–TiO_2 Interfaces: Ab Initio Time-Domain Study, ACS Nano 9 (2015) 11143–11155. https://doi.org/10.1021/acsnano.5b05843.

[30] Z. Xiao, Y. Yuan, Y. Shao, Q. Wang, Q. Dong, C. Bi, P. Sharma, A. Gruverman, J. Huang, Giant switchable photovoltaic effect in organometal trihalide perovskite devices, Nat. Mater. 14 (2015) 193–198. https://doi.org/10.1038/nmat4150.

[31] J.S. Park, S. Kim, Z. Xie, A. Walsh, Point defect engineering in thin-film solar cells, Nat. Rev. Mater. 3 (2018) 194–210. https://doi.org/10.1038/s41578-018-0026–7.

[32] H. Jin, E. Debroye, M. Keshavarz, I.G. Scheblykin, M.B.J. Roeffaers, J. Hofkens, J.A. Steele, It's a trap! On the nature of localised states and charge trapping in lead halide perovskites, Mater. Horizons 7 (2020) 397–410. https://doi.org/10.1039/C9MH00500E.

[33] D. Meggiolaro, F. De Angelis, First-Principles Modeling of Defects in Lead Halide Perovskites: Best Practices and Open Issues, ACS Energy Lett. 3 (2018) 2206–2222. https://doi.org/10.1021/acsenergylett.8b01212.

[34] D. Meggiolaro, S.G. Motti, E. Mosconi, A.J. Barker, J. Ball, C. Andrea Riccardo Perini, F. Deschler, A. Petrozza, F. De Angelis, Iodine chemistry determines the defect tolerance of lead-halide perovskites, Energy Environ. Sci. 11 (2018) 702–713. https://doi.org/10.1039/C8EE00124C.

[35] Y. Lei, Y. Xu, M. Wang, G. Zhu, Z. Jin, Origin, Influence, and Countermeasures of Defects in Perovskite Solar Cells, Small 17 (2021) 2005495. https://doi.org/https://doi.org/10.1002/smll.202005495.

[36] S.G. Motti, D. Meggiolaro, S. Martani, R. Sorrentino, A.J. Barker, F. De Angelis, A. Petrozza, Defect Activity in Lead Halide Perovskites, Adv. Mater. 31 (2019) 1901183. https://doi.org/https://doi.org/10.1002/adma.201901183.

[37] N. Li, S. Tao, Y. Chen, X. Niu, C.K. Onwudinanti, C. Hu, Z. Qiu, Z. Xu, G. Zheng, L. Wang, Y. Zhang, L. Li, H. Liu, Y. Lun, J. Hong, X. Wang, Y. Liu, H. Xie, Y. Gao, Y. Bai, S. Yang, G. Brocks, Q. Chen, H. Zhou, Cation and anion immobilization through chemical bonding enhancement with fluorides for stable halide perovskite solar cells, Nat. Energy 4 (2019) 408–415. https://doi.org/10.1038/s41560-019-0382-6.

[38] P. Zhu, S. Gu, X. Luo, Y. Gao, S. Li, J. Zhu, H. Tan, Simultaneous Contact and Grain-Boundary Passivation in Planar Perovskite Solar Cells Using SnO_2-KCl Composite Electron Transport Layer, Adv. Energy Mater. 10 (2020) 1903083. https://doi.org/https://doi.org/10.1002/aenm.201903083.

[39] L. Long, D. Cao, J. Fei, J. Wang, Y. Zhou, Z. Jiang, Z. Jiao, H. Shu, Effect of surface intrinsic defects on the structural stability and electronic properties of the all-inorganic halide perovskite $CsPbI_3$(0 0 1) film, Chem. Phys. Lett. 734 (2019) 136719. https://doi.org/https://doi.org/10.1016/j.cplett.2019.136719.

[40] W. Yang, J. Li, X. Chen, Y. Feng, C. Wu, I.D. Gates, Z. Gao, X. Ding, J. Yao, H. Li, Exploring the Effects of Ionic Defects on the Stability of $CsPbI_3$ with a Deep Learning Potential, ChemPhysChem 23 (2022) e202100841. https://doi.org/https://doi.org/10.1002/cphc.202100841.

[41] H. Xue, J.M. Vicent-Luna, S. Tao, G. Brocks, Compound Defects in Halide Perovskites: A First-Principles Study of $CsPbI_3$, J. Phys. Chem. C 127 (2023) 1189–1197. https://doi.org/10.1021/acs.jpcc.2c06789.

[42] N. Wang, Y. Wu, Intrinsic defects on α, γ and δ-$CsPbI_3$ (001) surfaces and implications for the α/γ to δ phase transition, Phys. Chem. Chem. Phys. 25 (2023) 16077–16085. https://doi.org/10.1039/D3CP00285C.

[43] M.F.N. Taufique, R. Khanal, S. Choudhury, S. Banerjee, Impact of iodine antisite (IPb) defects on the electronic properties of the (110) $CH_3NH_3PbI_3$ surface, J. Chem. Phys. 149 (2018) 164704. https://doi.org/10.1063/1.5044667.

[44] M.L. Agiorgousis, Y.-Y. Sun, H. Zeng, S. Zhang, Strong Covalency-Induced

Recombination Centers in Perovskite Solar Cell Material $CH_3NH_3PbI_3$, J. Am. Chem. Soc. 136 (2014) 14570–14575. https://doi.org/10.1021/ja5079305.

[45] J. Min, Y. Choi, D. Kim, T. Park, Beyond Imperfections: Exploring Defects for Breakthroughs in Perovskite Solar Cell Research, Adv. Energy Mater. 14 (2024) 2302659. https://doi.org/https://doi.org/10.1002/aenm.202302659.

[46] H. Uratani, K. Yamashita, Charge Carrier Trapping at Surface Defects of Perovskite Solar Cell Absorbers: A First-Principles Study, J. Phys. Chem. Lett. 8 (2017) 742–746. https://doi.org/10.1021/acs.jpclett.7b00055.

[47] J. Ran, B. Wang, Y. Wu, D. Liu, C. Mora Perez, A.S. Vasenko, O. V Prezhdo, Halide Vacancies Create No Charge Traps on Lead Halide Perovskite Surfaces but Can Generate Deep Traps in the Bulk, J. Phys. Chem. Lett. 14 (2023) 6028–6036. https://doi.org/10.1021/acs.jpclett.3c01231.

[48] J.-Y. Jeng, Y.-F. Chiang, M.-H. Lee, S.-R. Peng, T.-F. Guo, P. Chen, T.-C. Wen, $CH_3NH_3PbI_3$ Perovskite/Fullerene Planar-Heterojunction Hybrid Solar Cells, Adv. Mater. 25 (2013) 3727–3732. https://doi.org/https://doi.org/10.1002/adma.201301327.

[49] Y. Shao, Z. Xiao, C. Bi, Y. Yuan, J. Huang, Origin and elimination of photocurrent hysteresis by fullerene passivation in $CH_3NH_3PbI_3$ planar heterojunction solar cells, Nat. Commun. 5 (2014) 5784. https://doi.org/10.1038/ncomms6784.

[50] J. Xu, A. Buin, A.H. Ip, W. Li, O. Voznyy, R. Comin, M. Yuan, S. Jeon, Z. Ning, J.J. McDowell, P. Kanjanaboos, J.-P. Sun, X. Lan, L.N. Quan, D.H. Kim, I.G. Hill, P. Maksymovych, E.H. Sargent, Perovskite–fullerene hybrid materials suppress hysteresis in planar diodes, Nat. Commun. 6 (2015) 7081. https://doi.org/10.1038/ncomms8081.

[51] Y. Zhong, M. Hufnagel, M. Thelakkat, C. Li, S. Huettner, Role of PCBM in the Suppression of Hysteresis in Perovskite Solar Cells, Adv. Funct. Mater. 30 (2020) 1908920. https://doi.org/https://doi.org/10.1002/adfm.201908920.

[52] C. Rodríguez-Seco, M. Méndez, C. Roldán-Carmona, R. Pudi, M.K. Nazeeruddin, E.J. Palomares, Minimization of Carrier Losses for Efficient Perovskite Solar Cells through Structural Modification of Triphenylamine

Derivatives, Angew. Chem. Int. Ed. 59 (2020) 5303–5307. https://doi.org/https://doi.org/10.1002/anie.201915022.

[53] T. Gatti, E. Menna, M. Meneghetti, M. Maggini, A. Petrozza, F. Lamberti, The Renaissance of fullerenes with perovskite solar cells, Nano Energy 41 (2017) 84–100. https://doi.org/https://doi.org/10.1016/j.nanoen.2017.09.016.

[54] V. Ferguson, S.R.P. Silva, W. Zhang, Carbon Materials in Perovskite Solar Cells: Prospects and Future Challenges, Energy Environ. Mater. 2 (2019) 107–118. https://doi.org/https://doi.org/10.1002/eem2.12035.

[55] R.D. Chavan, B. Bończak, J. Kruszyńska, A. Mahapatra, M. Ans, J. Nawrocki, K. Nikiforow, P. Yadav, J. Paczesny, F. Sadegh, M. Unal, S. Akin, D. Prochowicz, Molecular Engineering of Azahomofullerene-based Electron Transporting Materials for Efficient and Stable Perovskite Solar Cells, Chem. Mater. 35 (2023) 8309–8320. https://doi.org/10.1021/acs.chemmater.3c01995.

[56] L. Jia, M. Chen, S. Yang, Functionalization of fullerene materials toward applications in perovskite solar cells, Mater. Chem. Front. 4 (2020) 2256–2282. https://doi.org/10.1039/d0qm00295j.

[57] S.M. Oner, D. Acikgoz, E. Sezen, E. Latifi, E. Demiroglu, I. Yavuz, C. Deger, Formation and Passivation of Surface Defects in Lead-Free Tin Halide Perovskites, J. Phys. Chem. C 128 (2024) 18962–18967. https://doi.org/10.1021/acs.jpcc.4c05298.

[58] M. Zhang, Q. Chen, R. Xue, Y. Zhan, C. Wang, J. Lai, J. Yang, H. Lin, J. Yao, Y. Li, L. Chen, Y. Li, Reconfiguration of interfacial energy band structure for high-performance inverted structure perovskite solar cells, Nat. Commun. 10 (2019) 4593. https://doi.org/10.1038/s41467-019-12613-8.

[59] Y. Xing, C. Sun, H.-L. Yip, G.C. Bazan, F. Huang, Y. Cao, New fullerene design enables efficient passivation of surface traps in high performance p-i-n heterojunction perovskite solar cells, Nano Energy 26 (2016) 7–15. https://doi.org/https://doi.org/10.1016/j.nanoen.2016.04.057.

[60] S. Shao, M. Abdu-Aguye, L. Qiu, L.-H. Lai, J. Liu, S. Adjokatse, F. Jahani, M.E. Kamminga, G.H. ten Brink, T.T.M. Palstra, B.J. Kooi, J.C. Hummelen, M. Antonietta Loi, Elimination of the light soaking effect and performance

enhancement in perovskite solar cells using a fullerene derivative, Energy Environ. Sci. 9 (2016) 2444–2452. https://doi.org/10.1039/C6EE01337F.

[61] T. Zheng, L. Fan, H. Zhou, Y. Zhao, B. Jin, R. Peng, Engineering of Electron Extraction and Defect Passivation via Anion-Doped Conductive Fullerene Derivatives as Interlayers for Efficient Invert Perovskite Solar Cells, ACS Appl. Mater. Interfaces 12 (2020) 24747–24755. https://doi.org/10.1021/acsami.0c04315.

[62] B. Li, J. Zhen, Y. Wan, X. Lei, Q. Liu, Y. Liu, L. Jia, X. Wu, H. Zeng, W. Zhang, G.-W. Wang, M. Chen, S. Yang, Anchoring Fullerene onto Perovskite Film via Grafting Pyridine toward Enhanced Electron Transport in High-Efficiency Solar Cells, ACS Appl. Mater. Interfaces 10 (2018) 32471–32482. https://doi.org/10.1021/acsami.8b11459.

[63] E. Castro, O. Fernandez-Delgado, F. Arslan, G. Zavala, T. Yang, S. Seetharaman, F. D'Souza, L. Echegoyen, New thiophene-based C_{60} fullerene derivatives as efficient electron transporting materials for perovskite solar cells, New J. Chem. 42 (2018) 14551–14558. https://doi.org/10.1039/C8NJ03067G.

[64] L. Przypis, T. Ahmad, K. Misztal, D. Honisz, E. Radicchi, E. Mosconi, W. Domagala, F. De Angelis, K. Wojciechowski, Designing New Indene-Fullerene Derivatives as Electron-Transporting Materials for Flexible Perovskite Solar Cells, J. Phys. Chem. C 125 (2021) 27344–27353. https://doi.org/10.1021/acs.jpcc.1c07189.

[65] Y. Li, Y. Zhao, Q. Chen, Y. (Michael) Yang, Y. Liu, Z. Hong, Z. Liu, Y.-T. Hsieh, L. Meng, Y. Li, Y. Yang, Multifunctional Fullerene Derivative for Interface Engineering in Perovskite Solar Cells, J. Am. Chem. Soc. 137 (2015) 15540–15547. https://doi.org/10.1021/jacs.5b10614.

[66] C. Quarti, F. De Angelis, D. Beljonne, Influence of Surface Termination on the Energy Level Alignment at the $CH_3NH_3PbI_3$ Perovskite/C_{60} Interface, Chem. Mater. 29 (2017) 958–968. https://doi.org/10.1021/acs.chemmater.6b03259.

[67] G. Kresse, J. Furthmüller, Efficient iterative schemes for ab initio total-energy calculations using a plane-wave basis set, Phys. Rev. B 54 (1996) 11169–11186. https://doi.org/10.1103/PhysRevB.54.11169.

[68] J.P. Perdew, K. Burke, M. Ernzerhof, Generalized Gradient Approximation Made Simple, Phys. Rev. Lett. 77 (1996) 3865–3868. https://doi.org/10.1103/PhysRevLett.77.3865.

[69] S. Osuna, M. Swart, M. Solà, Dispersion Corrections Essential for the Study of Chemical Reactivity in Fullerenes, J. Phys. Chem. A 115 (2011) 3491–3496. https://doi.org/10.1021/jp1091575.

[70] G. George, S. Posada-Pérez, Interaction of C_{60} with Methylammonium Lead Iodide Perovskite Surfaces: Unveiling the Role of C_{60} in Surface Engineering, Chem. Eur. J. 30 (2024) e202401283. https://doi.org/https://doi.org/10.1002/chem.202401283.

[71] D. Jain, S. Chaube, P. Khullar, S. Goverapet Srinivasan, B. Rai, Bulk and surface DFT investigations of inorganic halide perovskites screened using machine learning and materials property databases, Phys. Chem. Chem. Phys. 21 (2019) 19423–19436. https://doi.org/10.1039/C9CP03240A.

[72] H. Xue, G. Brocks, S. Tao, First-principles calculations of defects in metal halide perovskites: A performance comparison of density functionals, Phys. Rev. Mater. 5 (2021) 125408. https://doi.org/10.1103/PhysRevMaterials.5.125408.

[73] J.M. Crowley, J. Tahir-Kheli, W.A.I.I.I. Goddard, Resolution of the Band Gap Prediction Problem for Materials Design, J. Phys. Chem. Lett. 7 (2016) 1198–1203. https://doi.org/10.1021/acs.jpclett.5b02870.

[74] T. Umebayashi, K. Asai, T. Kondo, A. Nakao, Electronic structures of lead iodide based low-dimensional crystals, Phys. Rev. B 67 (2003) 155405. https://doi.org/10.1103/PhysRevB.67.155405.

[75] J. Even, L. Pedesseau, J.-M. Jancu, C. Katan, Importance of Spin–Orbit Coupling in Hybrid Organic/Inorganic Perovskites for Photovoltaic Applications, J. Phys. Chem. Lett. 4 (2013) 2999–3005. https://doi.org/10.1021/jz401532q.

[76] E. Mosconi, A. Amat, M.K. Nazeeruddin, M. Grätzel, F. De Angelis, First-Principles Modeling of Mixed Halide Organometal Perovskites for Photovoltaic Applications, J. Phys. Chem. C 117 (2013) 13902–13913. https://doi.org/10.1021/jp4048659.

[77] R.L.Z. Hoye, P. Schulz, L.T. Schelhas, A.M. Holder, K.H. Stone, J.D. Perkins, D. Vigil-Fowler, S. Siol, D.O. Scanlon, A. Zakutayev, A. Walsh, I.C. Smith, B.C. Melot, R.C. Kurchin, Y. Wang, J. Shi, F.C. Marques, J.J. Berry, W. Tumas, S. Lany, V. Stevanović, M.F. Toney, T. Buonassisi, Perovskite-Inspired Photovoltaic Materials: Toward Best Practices in Materials Characterization and Calculations, Chem. Mater. 29 (2017) 1964–1988. https://doi.org/10.1021/acs.chemmater.6b03852.

[78] R.E. Brandt, V. Stevanović, D.S. Ginley, T. Buonassisi, Identifying defect-tolerant semiconductors with high minority-carrier lifetimes: beyond hybrid lead halide perovskites, MRS Commun. 5 (2015) 265–275. https://doi.org/10.1557/mrc.2015.26.

[79] C.-J. Yu, Advances in modelling and simulation of halide perovskites for solar cell applications, J. Phys. Energy 1 (2019) 22001. https://doi.org/10.1088/2515-7655/aaf143.

[80] A.L. Montero-Alejo, F. Barría-Cáceres, L. Lodeiro, E. Menéndez-Proupin, Effective Interfaces between Fullerene Derivatives and $CH_3NH_3PbI_3$ to Improve Perovskite Solar Cell Performance, J. Phys. Chem. C 127 (2023) 41–51. https://doi.org/10.1021/acs.jpcc.2c06499.

[81] P.E. Blöchl, Projector augmented-wave method, Phys. Rev. B 50 (1994) 17953–17979. https://doi.org/10.1103/PhysRevB.50.17953.

[82] G. Kresse, D. Joubert, From ultrasoft pseudopotentials to the projector augmented-wave method, Phys. Rev. B 59 (1999) 1758–1775. https://doi.org/10.1103/PhysRevB.59.1758.

[83] G.E. Eperon, G.M. Paternò, R.J. Sutton, A. Zampetti, A.A. Haghighirad, F. Cacialli, H.J. Snaith, Inorganic caesium lead iodide perovskite solar cells, J. Mater. Chem. A 3 (2015) 19688–19695. https://doi.org/10.1039/C5TA06398A.

[84] Y.-H. Kye, C.-J. Yu, U.-G. Jong, K.-C. Ri, J.-S. Kim, S.-H. Choe, S.-N. Hong, S. Li, J.N. Wilson, A. Walsh, Vacancy-Driven Stabilization of the Cubic Perovskite Polymorph of $CsPbI_3$, J. Phys. Chem. C 123 (2019) 9735–9744. https://doi.org/10.1021/acs.jpcc.9b01552.

[85] O.T. Hofmann, E. Zojer, L. Hörmann, A. Jeindl, R.J. Maurer, First-principles

calculations of hybrid inorganic–organic interfaces: from state-of-the-art to best practice, Phys. Chem. Chem. Phys. 23 (2021) 8132–8180. https://doi.org/10.1039/D0CP06605B.

[86] R.F.W. Bader, Atoms in molecules, Acc. Chem. Res. 18 (1985) 9–15.

[87] X. Liu, Z. Yu, T. Wang, K.L. Chiu, F. Lin, H. Gong, L. Ding, Y. Cheng, Full Defects Passivation Enables 21% Efficiency Perovskite Solar Cells Operating in Air, Adv. Energy Mater. 10 (2020) 2001958. https://doi.org/https://doi.org/10.1002/aenm.202001958.

[88] J.-J. Yang, X.-Y. Liu, Z.-W. Li, T. Frauenheim, C. Yam, W.-H. Fang, G. Cui, The spin–orbit interaction controls photoinduced interfacial electron transfer in fullerene–perovskite heterojunctions: C_{60} versus C_{70}, Phys. Chem. Chem. Phys. 23 (2021) 6536–6543. https://doi.org/10.1039/D0CP06579J.